Research Square

Preprints are preliminary reports that have not undergone peer review.
They should not be considered conclusive, used to inform clinical practice,
or referenced by the media as validated information.

Reinforcement Learning-Driven Conversion Designed Minibinders to Small Molecules Targeting Porcine Nectin-1 IgV Domain for Anti-PRV Therapy

Zigong Wei

weizigong@163.com

Hubei University https://orcid.org/0000-0002-2445-6171

Lin Wei

Hubei University https://orcid.org/0000-0002-1977-2700

Yang Hu

Hubei University

Peng Chen

Hubei University

Yuhua Chen

Hubei University

Keke Wang

Hubei University

Jun Weng

Hubei University

Banbing Xing

Hubei University

Ke Ming

Hubei University

Zhiyong Wu

Hubei University

Miaomiao Geng

Hubei University

Zhang Liu

Hubei University

Guolin Wang

Hubei University

Yun You

Hubei University

Yihe Fang

Hubei University

Yanxia Liu

Hubei University

Wenxia Zhang

Hubei University

Haixia Xiang

Hubei University

Article

Keywords: minibinder, Nectin-1, protein-protein interaction (PPI) inhibitors, drug discovery, deep reinforcement learning

Posted Date: March 11th, 2026

DOI: https://doi.org/10.21203/rs.3.rs-8525913/v1

License: This work is licensed under a Creative Commons Attribution 4.0 International License. Read Full License

Additional Declarations: There is **NO** Competing Interest.

Abstract

The pseudorabies virus (PRV) is a devastating pathogen in swine with substantial economic impact and emerging zoonotic potential. Here, targeting the porcine Nectin-1 IgV domain, a critical mediator of PRV entry, five minibinders were designed to bind to hydrophobic surface, while **B1** achieve > 99% viral inhibition at concentrations > 500 nM with an EC_{50} of 1.2 nM *in vitro*. Capitalizing on the structural insights from **B1**, we implemented an artificial intelligence (AI)-driven reinforcement learning framework to convert the minibinder's pharmacophore into small-molecule inhibitors to block the protein-protein interactions (PPI). This approach yielded **SM1**, a compound exhibiting extraordinary potency and a high safety margin (EC_{50} = 0.42 pM; CC_{50} > 100 μM). *In vivo* studies demonstrated that both **B1** (6 mg/kg, BID) and **SM1** (30 mg/kg, BID) significantly reduced brain viral loads by > 99% in infected mice. This study not only identifies promising anti-PRV candidates targeting Nectin-1 but also establishes a generalizable AI-powered pipeline for developing small-molecule PPI inhibitors via minibinder-to-small-molecule conversion.

Introduction

The pseudorabies virus (PRV), a highly virulent swine alphaherpesvirus, causes acute disease characterized by fever and encephalomyelitis, leading to near 100% mortality in piglets. Serological surveillance indicated a significant rise in PRV positivity rates across China[1, 2]. This persistent epizootic inflicts substantial annual economic losses, estimated in the tens of billions of RMB in China, due to piglet mortality and stunted growth in fattening pigs. Critically, emerging PRV mutant strains pose a zoonotic risk[3], with human infections demonstrating close genetic links to swine strains[4], highlighting the urgent need for effective antivirals.

Nectin-1 (PVRL1), an immunoglobulin superfamily member, is a critical cellular receptor for PRV entry, functioning similarly to its role in Herpes Simplex Virus 1 (HSV-1) entry[5]. Soluble Nectin-1 fragments and antibodies can inhibit infection[6]. PRV glycoprotein D (gD) binds with high affinity directly to the IgV domain of both human and porcine Nectin-1[7–14]. This specific interaction, confirmed by structural studies (e.g., PDB 5X5W), is essential for initiating the membrane fusion process that allows PRV to enter host cells. Therefore, disrupting the gD-Nectin-1 interface presents a promising antiviral strategy[14]. Proof-of-concept comes from studies showing that engineered minibinders targeting PRV gD achieved potent inhibition (EC_{50} = 2.41 nM), demonstrating the therapeutic potential of blocking this crucial receptor-ligand interaction to combat PRV infection[15].

Recent breakthroughs in artificial intelligence (AI)-driven protein design (such as ProteinMPNN[16], RFdiffusion[17]) have significantly advanced the development of minibinders. These small functional proteins, typically around 8 kDa, represent promising alternatives to antibodies or nanobodies[18–20]. Minibinders have demonstrated considerable success in targeting diverse proteins for therapeutic applications, including anti-tumor, antiviral, and anti-inflammatory interventions. Notable examples include inhibitors against the SARS-CoV-2 spike protein receptor-binding domain[18], PRV gD[15], antagonists targeting IL-6R, GP130, and IL-1R1 receptor subunits[21], a Th17 antagonist[22], and inhibitors of the IL-2 receptor β chain[20]. This progress underscores the potential of minibinders as a versatile platform for targeting protein interfaces, including those involved in viral entry.

Minibinders represent an emerging class of therapeutic proteins offering distinct advantages. While promising studies indicate potential for oral bioavailability[22], significant challenges remain. Their pharmacokinetic (PK) properties, such as absorption, distribution, metabolism, and excretion (ADME), require further optimization. Furthermore, developing stable and efficacious formulations suitable for clinical application is an ongoing research

endeavor. Compared to more mature therapeutic modalities, minibinder development is relatively nascent, demanding comprehensive studies to fully unlock their therapeutic potential.

In contrast, small molecule drugs benefit from decades of development, resulting in mature manufacturing processes and well-understood theoretical principles[23]. Characterized by low molecular weight (< 1,000 Da), they constitute approximately 90% of marketed drugs.[24] A paramount advantage is their typically superior oral bioavailability, facilitating convenient administration and improved patient adherence[25]. Small molecules have proven highly successful in targeting well-defined binding pockets, such as those in protein kinases (e. g. gefitinib and erlotinib for EGFR-positive non-small cell lung cancer) and proteinases (e.g. imatinib for chronic myeloid leukemia). However, targeting protein-protein interactions (PPIs) presents a formidable challenge.[26–29] PPIs involve large, often flat and hydrophobic interfaces (typically 1500–3000 Å²) with shallow pockets[30–37]. These characteristics, such as flatness, featurelessness, complex topology, and shallow binding sites, render traditional small-molecule design strategies frequently ineffective[30, 31, 33, 35, 36]. The lack of known endogenous small-molecule ligands binding to these interfaces further hinders rational drug design efforts[30, 38], historically leading to the perception of many PPIs as "undruggable" targets[30, 33, 39].

To harness the well-established framework of small-molecule drug development while addressing the persistent challenges associated with PPI inhibition, here, we introduce a reinforcement learning (RL) [40]-guided synergistic strategy: employing minibinders, which offer high-resolution structural insights into target interfaces, to inform the rational design of small-molecule PPI inhibitors. RL, a branch of artificial intelligence, has proven increasingly influential in drug discovery due to its capacity to optimize decision-making through iterative environmental interactions, enabling efficient navigation of chemical space[41, 42]. When integrated with generative models, RL proves especially powerful in refining molecular architectures against biological targets, facilitating the de novo generation of compounds with predefined properties[43]. This approach has been empirically validated in our previous drug design campaigns[44, 45]. Here, with the structure and key interactions of designed minibinder targeting Nectin-1 set as predefined properties in the strategy, we demonstrate the conversion of minibinders into small-molecule inhibitors targeting the Nectin-1 IgV domain to develop anti-PRV agents. This integrated approach not only facilitates the rapid development of PRV therapeutics but also establishes a generalizable method for PPI drug discovery.

Results and discussion

Designed Minibinders.

Targeting the hydrophobic surface of the porcine Nectin-1 IgV domain (Fig. 1A), we employed a Rosetta-based computational pipeline (detailed in Section Experimental according to Cao et al.'s work[46]) Following rotamer interaction field (RIF) generation and initial scaffold placement, five minibinder candidates (**B1**-**B5**, detailed in Table 1) were designed. The structures predicted by AlphaFold2 (AF2) [47] shown that all designed minibinders adopted triple-helix bundle folds (about 60 amino acids, 6.24–6.72 kDa, Table 1) and successfully engaged the target hydrophobic surface as intended.

Consistent with our previous work[19, 20], we performed two independent 300 ns molecular dynamics (MD) simulations for all ten minibinder:Nectin-1 complexes (The binding modes predicted by AF2 were shown in **Fig. S1**) to assess binding stability. Root-mean-square deviation (RMSD) analysis of the minibinder backbones showed stability around 2–3 Å throughout the simulations (**Fig. S2**), confirming the conformational stability of the designs. Furthermore, root-mean-square fluctuation (RMSF) analysis indicated low flexibility (RMSF < 2 Å) for nearly all residues at the

minibinder:Nectin-1 interface (**Fig. S3**), supporting stable complex formation. The total binding free energy (ΔG_{bind}) were predicted using MM/GBSA method (Table 1). Among the initial five minibinders, **B1** exhibited the strongest predicted affinity (ΔG_{bind} = -54.35 kcal/mol), while affinities ranged from − 40.12 to -54.35 kcal/mol.

Table 1
Molecular wights, and binding energies for the all designed minibinders.

ID	Sequence	Molecular wight (kDa)	ΔG_{bind} predicted by MM/GBSA (kcal/mol)
B1	SEIEALARAAHELLDQLQAAGVISEEAAAELRAILDEAIELGNLSLVESIYQSLKTFVAQA	6.50	-54.35 ± 8.44
B2	DLFHEFAELHKRIAHLAKEGDREEAKKLLEELRRVAEEANSPEAEKVVKLLEEFLR	6.61	-52.46 ± 7.02
B3	NKEELKKIIEEVKELQKKGLISDEMAKAIVEAAKLGIEKNDPALVELAKSLLNSAKTFINS	6.72	-51.21 ± 8.27
B4	SHEEAERLFHEAVALLMQGDREEARKLIERLEELAEKSNDPRIRRAVEDLKKLLKF	6.66	-49.21 ± 8.23
B5	AAVEEVEKLVEEALKTKDPKKQKKLIEEARKLAEEAGNQALLEYVESQARSLKLF	6.24	-40.12 ± 7.11

Expression, purification, in vitro and in vivo test for minibinders.

The characterization of minibinders.

Based on the computational predictions, **B1**-**B5** were selected for experimental validation. Each was expressed in *Escherichia coli* BL21(DE3) using a bacterial expression system, taking advantage of the well-established suitability of prokaryotic hosts for producing small, stable, single-domain protein[48]. The primers are detailed in **Table S1**. Following expression, the minibinders were purified by immobilized metal affinity chromatography (IMAC, Ni-NTA) followed by size-exclusion chromatography (FPLC). SDS-PAGE analysis confirmed successful expression and high purity with high purity, and molecular weights between (6–7 kDa, **Fig. S4**), consistent with theoretical predictions. To evaluate secondary structure composition and thermal stability, circular dichroism (CD) spectroscopy was performed at various temperatures. The CD spectra indicated that the 5 minibinders consisted of only α-helices, aligning with the computational design models. Notably, even after exposure to 95°C, each minibinder retained its structural integrity, demonstrating exceptional thermostability (**Fig. S5**).

In vitro anti-PRV activities of the minibinders.

The anti-PRV activities of the binders were assessed on PK15 cells, a well-established cell line for PRV infection. Viral load was quantified by qPCR, and the inhibitory rate was calculated. Concentration-response curves are presented in Fig. 1C. The EC_{50} for **B1** is 1.2 nM, while **B2** is 114.1 nM, **B3** is 7.1 nM, **B4** is 17.1 nM, **B5** is 19.0 nM. Notably, **B1** demonstrated the highest potency, achieved > 99% viral inhibition at concentrations ≥ 500 nM (Fig. 1C). cytopathic effect (CPE) analysis demonstrated that PRV-induced syncytium formation was almost completely blocked when the concentrations of **B1** were not less than 31.25 nM. (Fig. 1D) The 50% cytotoxic concentration (CC_{50}) of **B1** > 50 μM (Fig. 1E), which show > 7000 -fold drug safety margin.

The dissociation constant K_D of **B1** for binding to Nectin-1 IgV domain (the details for expression and purification shown in **Supplementary information**) is 44.5 μM (Fig. 1F), demonstrating the ability of **B1 to** bind Nectin-1, although the dimerization of Nectin-1[49] led by the strong hydrophobicity may interferes with accuracy of BLI assay. To futher explore the target of the **B1**, we evaluated the effect of the mini-binders in PK15 cells on viral attachment and entry. The 1 μM of **B1** treatment significantly inhibited viral attachment and entry compared to the phosphate buffer saline (PBS)-treated control, while 0.5 μM of **B1** showed weaker activity (**Fig. S6**). As Nectin-1 plays a crucial role in the early stages of PRV infection by facilitating viral entry into host cells, this also suggested that **B1** can block PRV infection by targeting Nectin-1:gD interactions.

In vivo efficacy of **B1**.

The *in vivo* efficacy of **B1** was evaluated in a murine PRV model. Mice received **B1**(6 mg/kg; twice daily, BID; intraperitoneal, IP) or vehicle control (n = 5). 2 mice in the treatment group survived within 7.5-day study period, while 3 died on day 7. In contrast, in the vehicle group, one mouse in the vehicle group died on day 5, four died on day 6 (Fig. 1G), resulting in a survival rate of 40% for the treatment group vs. 0% for the vehicle group. However, quantification of brain viral loads at the study endpoint revealed markedly lower levels in the **B1** group (1.7×10^3-2.6×10^4 copies/g), compared to the vehicle group (3.8×10^5-4.8×10^7 copies/g) (**Table S2)**, representing a > 99% reduction *in viral* burden, Statistical analysis confirmed the highly significant protective effect of **B1** (P = 0.0005; Fig. 1H).

Covet B1 to Small Molecules.

Deep reinforcement learning protocol.

Designing small molecules targeting the Nectin-1:gD PPI interface presents a formidable challenge due to its large, flat, and hydrophobic nature (2761 Å² around gD in PDB 5X5W, shown in **Fig. S7**, calculated by PyMOL v2.1, https://github.com/schrodinger/pymol-open-source) with shallow pockets. The lack of known endogenous small-molecule ligands binding to these interfaces further hinders rational drug design efforts. Leveraging the advantages of small-molecule drugs and guided by the key interactions identified in the **B1**:Nectin-1 complex, we developed a deep RL-driven pipeline to convert the minibinder pharmacophore into small-molecule inhibitors to enhance the anti-PRV effect. This approach addresses the historical challenge of targeting flat, featureless PPI interfaces like Nectin-1's gD-binding site by utilizing the minibinder's structure and key interaction map as a blueprint. Our protocol integrates fragment-based design, transfer learning (TL), and RL (Fig. 2A, details in Section Experimental). Briefly, critical tripeptide fragments from **B1**'s binding interface were extracted and encoded. A pre-trained generative model (RNN architecture) was fine-tuned on these fragments and then deployed within an RL framework. The RL reward function incorporated: (1) alignment with the 3D pharmacophore derived from **B1**'s key interactions (hydrophobic patches, H-bonds, electrostatic), (2) predicted binding affinity (docking score), and (3) drug-likeness constraints (e.g., molecular weight penalty: 200–600 Da). This multi-objective optimization aimed to generate small molecules mimicking **B1**'s critical binding features while maintaining favorable properties.

Key Interactions of **B1** *with Nectin-1.*

The crystal structure of the gD-Nectin-1 complex (PDB 5X5W), highlights the hydrophobic nature of their interaction interface, guiding our initial minibinder design strategy. Building on the experimental validation of **B1** as a potent inhibitor, we analyzed its computationally predicted binding mode to Nectin-1 (Fig. 3A-C) to identify key interactions for guiding small-molecule design. Analysis revealed a binding network (value of binding energy contributions < -1.00 kcal/mol) of polar and hydrophobic: GLU30 (**B1)** forms an electrostatic interaction with LYS25 (Nectin-1); SER49 (**B1)**

forms hydrogen bonds with ASN97, GLN28 (Nectin-1). GLN52 and THR56 (**B1)** formed hydrogen bonds with ASN41 and SER52 (Nectin-1), respectively. Crucially, extensive hydrophobic interactions were observed involving residues LEU41, ILE34, ILE50, ILE23, ALA27, LEU31, and PHE57 in **B1** packing against THR27, ALA91, PHE93, PRO94, MET49, and ILE44 in Nectin-1, (Fig. 3A-C) a crucial factor influencing protein interactions[50], strongly correlated with the success rate of binder design highlighted by Cao et al.'s work[51]. MM/GBSA-based residue energy decomposition quantified this contribution in **B1**-binding to the hydrophobic amino acids ILE44, MET49, LEU54, PHE93, and PRO94 in Nectin-1 totaled approximately 16.12 kcal/mol, accounting for 30% of the total binding energy. And in the designed binder **B1**, the analogous hydrophobic residues ILE23, ILE34, ILE50, and PHE57 contributed 13.20 kcal/mol, representing about 25% of the total binding energy. (Fig. 3C and **Table S3**) These analyses confirm the dominance of hydrophobic effects at the **B1**:Nectin-1 interface, providing critical pharmacophore constraints for subsequent small-molecule design (defined by RDKit, see Section Experimental).

Small molecules morph form binder by deep reinforcement learning protocol.

During RL, the model's performance was monitored, with the average reward stabilizing around 0.60, and the numbers of scaffolds stabilizing around 60. (**Fig. S8**A, B). Sampling from the final RL model yielded 20,000 unique molecules (98% valid SMILES, 63% uniqueness rate). These generated molecules were compared with the ChEMBL_36[52, 53] database using the maximum Tanimoto coefficient (TC) calculated from Morgan fingerprints[54]. The TC values were primarily distributed between 0.5 and 0.8, with a median of 0.63 (Fig. 2C), indicating substantial novelty of the generated compounds. Subsequently, the compounds were docked into the Nectin-1 binding site, which defined as a 20 Å sphere centered on the protein–protein interface to encompass its full extent, by AutoDock Vina, generating 10 poses per molecule. The resulting Vina scores ranged from − 4.0 to 2.0 kcal/mol, with a median of -1.77 kcal/mol (Fig. 2D), suggesting that over half of the molecules exhibit potential high binding affinity. These potentially high affinity molecules (Vina Score <-2 kcal/mol) retained considerable novelty, as reflected by a median TC of 0.59 and a distribution mainly between 0.4 and 0.8 (Fig. 2E) The quantitative estimate of drug-likeness (QED) for the generated compounds was predominantly distributed between 0.2 and 0.6, with a median of 0.39, and 27% of all exceeded 0.5, (Fig. 2F) indicating acceptable drug-likeness. Max TCs, Vina Score and QED for each compound were visualized via a uniform manifold approximation and projection (UMAP) (Fig. 2B), revealing a broad chemical space.

The docking poses of top 1000 compounds underwent visual inspection, focusing on identification of druggable compounds that featured diverse molecular backbones, plausible binding poses, synthetic accessibility, and at least three hydrogen bonds and/or π-interactions with key interface residues. This process identified 56 "prefect" hit compounds (see **Supplementary information**). Interaction analysis of the top 30 hits (Fig. 2G) revealed their ability to engage key Nectin-1 residues: most formed hydrogen bonds with ASN41 (**h1-h6**, **h8**-**h11**, **h13**-**h19**, **h21**, **h22**, **h25**, **h28**-**h30**), ASN97 (**h1-h4**, **h6**, **h7**, **h9**-**h11**, **h14**, **h15**, **h18**-**h21**, **h24**, **h26**-**h29**), GLN28 (**h4**, **h5**, **h9**, **h12**, **h16**, **h18**, **h19**, **h22**, **h24**, **h25**, **h29**), SER52(**h25**), and formed π-π or hydrogen-π interactions with PHE93 (**h1**-**h7**, **h9**, **h12-h16, h19**-**h21**, **h23**, **h27-h28**, **h30**), GLN28(**h8**, **h12**, **h17**, **h23**, **h26**). Additionally, they can also formed H-bonds with GLU89 (**h4**, **h8**, **h10, h12**-**h18**, **h20**, **h23**, **h24**, **h26**, **h28**-**h30**) GLN32 (**h5**, **h12**, **h13**, **h16**, **h23**, **h24**, **h27**, **h29**), LYS39 (**h2**, **h8**, **h12**, **h15**, **h20**, **h28**, **h29**), THR27 (**h3**, **h5**-**h7**, **h10**, **h13**, **h21**, **h23**, **h27**, **h30**), GLU99 (**h8**, **h17**, **h18**, **h26**),THR30 (**h4,h10**, **h14**), and formed H-π, Cation-π or π-π interactions were observed with LYS39 (**h6**, **h8**-**h11**, **h14**, **h17**, **h19, h21**, **h22**, **h24**-**h26**, **h28**, **h29**). (Fig. 3D and **Fig. S9**)

Notably, **h29**, a synthetic-friendly compound, its predicted binding mode (Fig. 3D) showed hydrogen bonds with GLN28, ASN41, GLN32, GLU89, and ASN97. Ethyl forms hydrophobic interactions with ALA91 and others. Like other PPI interfaces, Necitn-1 has a large region of interface and is a ligand-free protein, which lacks a deep, well-defined

pocket, making it difficult to develop small molecule inhibitors (Fig. 3E). Crucially, **h29** binds directly at the expansive Nectin-1:gD PPI interface (Fig. 3E). The molecule appears **"**suspended" above the surface (Fig. 3F), an achievement difficult to realize with conventional pocket-based drug discovery. This successful engagement of a traditionally "undruggable" flat interface underscores the power of minibinder-guided small-molecule design.

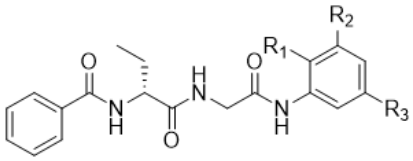
In vivo and in vitro test for analogs of **h29**.

Structure-Activity Relationship (SAR) Analysis of **SM1**-**SM6**.

Based on the docking predicted binding pose of **h29** (Fig. 3D), we can determine that the hydrogen bond formed by the -OH of R_1 as both a donor and acceptor is very important. As shown in Table 2 and Fig. 4A, the activity lost > 10-fold potency when -OH (**SM1**, 0.42 pM) was replaced by -F (**SM2**, 5.30 pM), indicating H-bonding donor capacity. Halogens (-Cl/-Br, **SM3/SM4**) reduced activity > 4,000-fold, confirming the inadequacy of hydrophobic/halogen-bonding motifs. For R_2 group, methyl substitution (**SM1**) was essential; replacement by -Cl (**SM6**) decreased potency 120-fold, respectively, suggesting steric and hydrophobic constraints in the subpocket. Fluorine at meta-position (**SM5**) compromised activity (EC_{50} = 85.58 pM), confirming ortho-position specificity for R_1. **SM1** showed the highest anti-PRV activity among the 6 analogs. CPE analysis demonstrated that PRV-induced syncytium formation was almost completely blocked when the concentrations of **SM1** were not less than 12.8 pM. (Fig. 4B) The CC_{50} of **SM1** > 100 μM (Fig. 4C), which show > 2 million-fold drug safety margin.

The K_D of **SM1** for binding to Nectin-1 IgV domain is 7.3 μM(Fig. 4D**)**, indicating a stronger binding ability to Nectin-1 than **B1**, within the limitations of the BLI assay. To futher explore the target of the **SM1**, we also evaluated the effect of the mini-binders in PK15 cells on viral attachment and entry. 0.25 μM of **SM1** also can significantly inhibited viral attachment and entry (**Fig. S6**), which also suggested that **SM1** block PRV infection by targeting Nectin-1:gD interactions.

Table 2. Anti-PRV activity of **SM1–SM6** in PK15 cells.



ID	R_1	R_2	R_3	EC_{50} (pM)
SM1	OH	CH_3	H	0.42 ± 0.05
SM2	F	CH_3	H	6.56 ± 0.54
SM3	Cl	CH_3	H	(2.48 ± 1.08)×10^3
SM4	Br	CH_3	H	(1.98 ± 0.71)×10^3
SM5	H	CH_3	F	85.58 ± 9.50
SM6	OH	Cl	H	50.28 ± 19.19

Pharmacokinetics of **SM1**.

The *in vivo* pharmacokinetic (PK) evaluation of **SM1** was conducted in Kunming mice after a single IP dose (30 mg/kg). The PK parameters are provided in Fig. 4E, Table 3 and **Supplementary information**. Compound **SM1** reached the maximum concentration (Cmax, 4.46 μg/mL) at 0.25 h, The area under the curve (AUC_{0-t}) of **SM1** were 5.12 μg/mL, at an IP injection dose of 30 mg/kg, and the half-life of it was 0.49 h. Plasma concentrations exceeded the *in vitro* EC_{50} (0.42 pM) for > 8 h (Fig. 4E), supporting BID dosing for efficacy studies.

Table 3. PK Parameters of **SM1** in mice.

		Parameters
Animals		Kunming mice
Administration		IP
Dose, mg/kg		30
Pharmacokinetic Parameters	$T_{1/2}$ (h)	0.49
	T_{max} (h)	0.25
	C_{max} (μg/mL)	4.46
	AUC_{0-t} (μg·h·mL^{-1})	8.60
	$AUC_{0-\infty}$ (μg·h·mL^{-1})	9.53
	MRT_{0-t} (h)	5.12
	$MRT_{0-\infty}$ (h)	8.33

Pharmacodynamics of **SM1**.

We evaluated the ability to modulate PRV in the mice at 30 mg/kg BID (IP, n = 5). 4 mice in the treatment group survived within 7.5-day study period, while one died on day 7. In contrast, in the vehicle group, one mouse in the vehicle group died on day 5, three died on day 6, and one died on day 7. **SM1** significantly improved survival (80% vs. 0% in vehicle, Fig. 5A), significantly better than **B1**, although it also conferred partial protection. Examination of PRV copies in the brains of deceased or euthanized mice revealed 9.5×10^{5}-1.6×10^{10} copies/g in the vehicle group, compared to only 2.8×10^{2}-2.3×10^{3} copies/g in the treated group. This represented a > 99% inhibition rate, demonstrating a significant effect (P = 0.0003). (Fig. 5B and **Table S2**)

The characterization and effects of **SM1***-treated mice.*

To evaluate the effects of SM1 on PRV-induced inflammatory response, the expression of IL-1β, IL-6, and TNF-α, in brain were determined. The results showed that the PRV led to increased expression of IL-1β (74-fold), IL-6 (16-fold), and TNF-α (67-fold) compared to normal levels. In the **SM1**-treatment group, the expression of IL-1β (4-fold), IL-6 (similar level), and TNF-α (8-fold) were close to normal levels (Fig. 5C and **Table S4**), indicating that **SM1**-treated significantly suppressed the mRNA levels of these pro-inflammatory cytokines, suggesting remarkable antiinflammation effects. Representative HE staining results showed that the pathological features of extensive hemorrhage with prominent lymphocytic infiltration observed in the **SM1**-treated group were markedly reduced compared with those in the vehicle control group (indicated by yellow arrows).(Fig. 5D)

Targeting Nectin-1 can inhibit PRV.

To our knowledge, this work represents the first report of therapeutic agents (**B1** and **SM1**) specifically targeting the Nectin-1 IgV domain. Structural analyses have shown that Nectin-1 homodimerization is mediated through its IgV domain, a region conserved across swine and humans[49], and that PRV gD binds to this same domain in a manner that mimics the homodimer interface.[10] Previous work has demonstrated that co-application of Nectin-1 and PRV gD monoclonal antibodies effectively blocks PRV infection,[55] further supporting the potential of Nectin-1 as a therapeutic target. Here, we designed the mini-binders and small compounds to bind precisely at the gD interaction site on Nectin-1, thereby competitively inhibiting gD binding and disrupting Nectin-1 self-interaction. Binding to Nectin-1 was confirmed by both affinity measurements (K_D) and anti-RRV assays. Therefore, the safety profile of the designed Nectin-1 minibinders requires careful evaluation, though they may prove safe in certain contexts. In addition, further experiments, such as determining complex crystal structures, are needed to fully validate the targeting ability of **SM1** and **B1**.

Minibinder-to-small-molecule conversion can help to design Nectin-1 PPI inhibitors.

In this RL work, we extracted key interaction features from the binding mode of minibinder, **B1**, to construct a pharmacophore model, combined with a Vina score-based activity prediction, which served as the reward function to guide the generation of bioactive molecules. As exemplified by compound **h29**, which engages critical interface residues as described above. And its optimized analog **SM1**, which shows high potency both *in vitro* and *in vivo*, the minibinder effectively highlights specific amino-acid hotspots at the expansive PPI interface, enabling focused and rational inhibitor design. This strategy is particularly valuable for PPIs that lack prior inhibitor scaffolds or high-affinity leads. Moreover, our RL-driven de novo design offers a distinct advantage in exploring novel chemotypes. Comparison with the ChEMBL_36 database revealed that more than half of the generated compounds exhibit considerable structural novelty (TC < 0.6, Fig. 2C). Notably, among molecules with Vina scores below − 2 kcal/mol, over half also qualify as new chemical entities (TC < 0.6, Fig. 2E). These results demonstrate that our approach can effectively expand the accessible chemical space for developing inhibitors against challenging targets such as Nectin-1. Further case studies are currently underway to assess the broader applicability of this methodology.

Conclusion

In conclusion, this study establishes Nectin-1 as a druggable target for anti-PRV therapy through an innovative de novo design strategy. By computationally targeting the hydrophobic IgV domain of porcine Nectin-1, we successfully developed minibinder **B1**, a 6.50 kDa helix bundle, which potently inhibits PRV infection (EC_{50} = 1.2 nM) and > 99% viral load reduction *in vivo*. Furthermore, by leveraging an AI-driven reinforcement learning pipeline guided by **B1**'s interaction pharmacophore, we generated the small-molecule inhibitor **h29**. **SM1**, an analog of **h29**, demonstrates remarkable potency, an excellent safety profile (EC_{50} = 0.42 pM, CC_{50} > 100 μM), achieving > 99% brain viral clearance *in vivo* (30 mg/kg BID). BLI assays and PRV assays studies suggested the two agents disrupt PRV infection by blocking viral attachment and entry via Nectin-1:gD interface inhibition.

Beyond delivering the first-reported Nectin-1-targeted antivirals, this work pioneers a generalizable framework for tackling traditionally "undruggable" protein-protein interfaces. Our minibinder-to-small-molecule conversion paradigm, validated from *in vitro* assays to *in vivo* models, offers a promising strategy for the discovery of PPI inhibitors against challenging therapeutic targets.

Materials and methods

Design of minibinders against PRV IgV domain.

The crystal structure of swine Nectin-1 bound to PRV gD (PDB: 5X5W) served as our design template. We followed the methodologies described by Cao et al.[46], Amino acids within the structure were refined using Rosetta FastRelax (15 cycles, beta_nov16_cart scoring function) to eliminate unfavorable conformations. Key interacting residues between gD (e. g., MET201-ARG202, PRO206-TYR208, VAL216, and TYR219) and the Nectin-1 IgV domain (e. g., THR63-GLN64, GLN76-ASN77, ILE80, SER88, LEU90-ALA91, ALA127-PRO130, ASN133)[10] were identified (Fig. 1A). Minibinder design focused on the hydrophobic surface of the receptor. In the Nectin-1 IgV domain, seven hydrophobic amino acids (VAL24, ILE26, PRO47, MET49, THR92, PHE93, PRO94) formed a highly hydrophobic surface and were selected as key hotspots. A rotamer interaction field (RIF) was generated around selected hotspots. 1,000 structurally diverse, stable protein scaffolds were docked against VAL24, PRO47, MET49, PHE93, and PRO94 using PatchDock[56]. High-resolution refinement aligned scaffold-derived motif backbones with target residues, optimizing side chains for minimal monomer energy (58,310 configurations generated).

The subsequent steps of interface design, scaffold motif extraction, clustering, and grafting were executed to refine scaffold residues at the target interface for enhanced binding affinity in accordance with the protocols outlined by Cao et al.[56]. Rosetta design protocols mutated scaffold residues within 10 Å of the interface while restricting distal positions (> 10 Å) to rotamer optimization. Target residues within 10 Å of scaffolds underwent rotamer sampling, with all backbones and core side chains fixed. Complexes were prioritized using multi-parameter metrics: binding energy, shape complementarity, residue-specific scores, and SAP_score. This yielded 34,980 candidates, filtered by the threshold criteria: contact_molecular_surface > 450 Å; ddg < -30; binder_delta_sap > 12; mismatch_probability < 0.1; sap_score < 35; score_per_res < -2.4. Filtered candidates were ranked by ddg, contact_patch, target_delta_sap, and contact_molec_sq5_apap_target to select 5 top-ranked binders (**B1**-**B5**) for further evaluation. The model for each complex of the all 5 candidates was verified by AF2[47] and then relaxed by molecular dynamics simulation with 300 ns and the free energies were carried out according in our previous work[19].

Deep Reinforcement Learning Driven Minibinder to Small-Molecule Conversion for Nectin-1 inhibitors.

Our protocol integrates fragment-based design, transfer learning, and reinforcement learning (RL) (Fig. 2A). The conversion protocol employed XREINVENT[45] (https://github.com/weilin199204/xdalgorithm_XtalPi_copy) to transform **B1**'s binding motifs into small molecules. First, Key tripeptide fragments were extracted from minibinder residues within 3.5 Å of Nectin-1 with assembly rules: isolated blocks with 1-residue incorporated flanking neighbors; consecutive blocks with 2-residues extended by next one neighbor residue; contiguous blocks of ≥ 3 residues formed standalone fragments using a sliding window approach (resdue 1-2-3, 2-3-4, etc.) (details see **Supplementary information**). These tripeptides were encoded as SMILES strings with ring/branch notation and converted to one-hot vectors. The generative model was built with a 3-layer of Gated Recurrent Unit (GRU)[57], a type of recurrent neural network (RNN)[58]. The final linear layer is defined by the vocabulary, which is determined by identifying all unique tokens during dataset processing. Finally, a softmax transformation is applied to provide the token probability distribution.

Transfer learning(TL) initialized the model: first pretraining on clustered ChEMBL as our previous work[59], then fine-tuning on the tripeptide dataset (batch size = 128, 500 epochs, learning rate = 5×10^{-4}). This yielded a focused prior model generating peptide-inspired scaffolds. The input file is provided in the Zenodo (https://zenodo.org/records/16986879).

Here, in RL a multi-parameter objective (MPO) ranges from 0 to +∞. The MPO score ($MPO\left(S\right)_{score}$) is combined with the prior's likelihood to calculate negative log-likelihood (NLL) of the augmented likelihood:

$$NLL\left(\varvec{S}\right)_{Augmented} = NLL\left(\varvec{S}\right)_{Prior} + \sigma\, MPO\left(S\right)_{score} \quad (1)$$ [43, 60]

Score of 3D pharmacophore, S_{pharm} measured by RDKit, and the target 3D pharmacophore defined according **B1** as our precious work[44]. The OE2 of GLU30, OG of SER49, OE1 of GLN52 and OG1 of THR56 were defined as hydrogen bond donor or accepter. ILE34, ILE50, ILE23, and PHE57 were defined as hydrophobic pharmacophore. Vina Score is the docking scores to predict binding affinity,

$$\mathrm{S}_{docking} = \frac{Vina\ Score}{-5}$$

2

$MPO\left(S\right)_{score}$ were evaluated by a multiobjective reward function:

$$MPO\left(S\right)_{score} = \frac{4\mathrm{S}_{docking} + 4\mathrm{S}_{3d-pharm} + S_{mw}}{9}$$

3

Where S_{mw} imposed molecular weight constraints (200–600 Da) via double sigmoid:

$$S_{mw} = \frac{10^{a*\frac{MW}{c}}}{10^{a*\frac{MW}{c}} + 10^{a*\frac{l}{c}}} - \frac{10^{b*\frac{MW}{c}}}{10^{b*\frac{MW}{c}} + 10^{b*\frac{h}{c}}},\ a = b = 20, c = 600$$

4

Agent loss is minimized to prioritize molecules balancing bioactivity, structural mimicry, and drug-like properties. Penalties enforced scaffold diversity during 500-epoch training (learning rate = 0.0001), with 64 SMILES strings per batch, and σ = 128.0 scaling likelihood contributions. The outputted 20,000 compounds underwent docking and visual inspection, yielding 11 validated hits. The input file is provided in the Zenodo (https://zenodo.org/records/16986879). More information can be obtained from **Supplementary information** and the Olivecrona and Blaschke ‘s work[43, 60].

Reagents

PK15 cells were stored in our laboratory[61] and cultured with fresh Dulbecco's modified Eagle's medium (DMEM) (No. 11965092, Gibco™) with 10% fetal bovine serum (FBS) (No. P30-3306, PAN™) and 1% penicillin-streptomycin solution (100X, No. BL505A, Biosharp™) at 37°C, incubated at a mixture of 5% CO_2 and 95% atmosphere. PRV was isolated from a pig farm in Hubei Province, China, whose DNA pol was identical to the HuBXY/2018 strain.

^{1}H NMR and ^{13}C NMR spectra were recorded on a Bruker Bruker Avance III 400M spectrometer using solvents as indicated (DMSO-d_6). Chemical shifts were reported in d values (ppm) with TMS as the internal reference, and *J* values were reported in hertz (Hz); signals are abbreviated as s (singlet), d (doublet), t (triplet), and m (multiplet). Mass spectra were recorded on an LC Auto sampler device Agilent Technologies 6224 TOF or 6540 TOF LC/MS

instrument. TLC was performed on SepaBean Machine T (Santai Technologies) for TLC and spots were visualized by irradiation with UV light (254 nm and 365 nm). Flash column chromatography was performed on columns packed with Silica Gel (200–300 mesh, Qingdao Haiyang Chemical Company). Solvents were of reagent grade and were purified and dried by standard methods when necessary. The purity of target compounds > 95%, which was determined by analytical HPLC with HPLC conditions: methanol:water 45:55(v:v); flow rate 1.0 mL/min; UV detection from 210 to 400 nm; temperature, ambient; injection volume, 20 μL (Shimadzu LC-2505 CN) The characterization data of target compounds were described in **Supplementary information.**

(R)-N-(1-((2-((2-hydroxy-3-methylphenyl)amino)-2-oxoethyl)amino)-1-oxobutan-2-yl)benzamide (**SM1**) (98.13% purity, 17.9% yield) ^{1}H NMR (400 MHz, DMSO-d_6, δ) 9.49 (s, 1H), 8.96 (s, 1H), 8.54 (d, *J* = 7.5 Hz, 1H), 8.45 (t, *J* = 5.8 Hz, 1H), 7.96–7.87 (m, 2H), 7.60–7.51 (m, 1H), 7.48 (dd, *J* = 8.2, 6.6 Hz, 2H), 7.39–7.31 (m, 1H), 6.92 (d, *J* = 7.3 Hz, 1H), 6.73 (t, *J* = 7.7 Hz, 1H), 4.40 (ddd, *J* = 9.0, 7.5, 5.4 Hz, 1H), 4.09–3.89 (m, 2H), 2.18 (s, 3H), 1.97–1.68 (m, 2H), 0.96 (t, *J* = 7.4 Hz, 3H).^{13}C NMR (400 MHz, DMSO-d_6, δ) 172.97, 169.32, 167.29, 146.93, 134.47, 131.85, 128.66, 128.06, 127.42, 126.55, 126.45, 121.03, 119.70, 55.68, 43.21, 25.18, 16.95, 11.23. HRMS (ESI) m/z: $[M + H]^+$ calcd for $C_{20}H_{24}N_3O_4$, 370.17613; found, 370.17742.

(R)-N-(1-((2-((2-fluoro-3-methylphenyl)amino)-2-oxoethyl)amino)-1-oxobutan-2-yl)benzamide (**SM2**) (97.61% purity, 19.4% yield) ^{1}H NMR (400 MHz, DMSO-d_6, δ) 9.54 (s, 1H), 8.46 (d, *J* = 7.6 Hz, 1H), 8.33 (t, *J* = 5.9 Hz, 1H), 7.92 (d, *J* = 7.7 Hz, 2H), 7.66 (d, *J* = 7.5 Hz, 1H), 7.59–7.50 (m, 2H), 7.48 (d, *J* = 7.5 Hz, 1H), 7.11 (dq, *J* = 13.0, 4.2 Hz, 1H), 6.96 (d, *J* = 7.1 Hz, 1H), 4.41 (td, *J* = 8.3, 5.4 Hz, 1H), 3.98 (q, *J* = 8.0 Hz, 2H), 2.26 (s, 3H), 1.87 (dq, *J* = 13.9, 7.1 Hz, 1H), 1.82–1.69 (m, 1H), 0.96 (t, *J* = 7.4 Hz, 3H). ^{13}C NMR (400 MHz, DMSO-d_6, δ) 172.83, 168.51, 167.14, 153.48, 151.07, 134.52, 133.88, 131.81, 128.64, 128.04, 125.75, 124.75, 115.64, 55.60, 43.05, 25.23, 20.92, 11.20. HRMS (ESI) m/z: $[M + H]^+$ calcd for $C_{20}H_{23}FN_3O_3$, 372.1718; found, 371.1968.

(R)-N-(1-((2-((2-chloro-3-methylphenyl)amino)-2-oxoethyl)amino)-1-oxobutan-2-yl)benzamide (**SM3**) (97.88% purity, 33.1% yield) ^{1}H NMR (400 MHz, DMSO-d_6, δ) 9.33 (s, 1H), 8.51 (d, *J* = 7.7 Hz, 1H), 8.46 (t, *J* = 5.8 Hz, 1H), 7.95–7.86 (m, 2H), 7.65 (dd, *J* = 8.1, 1.7 Hz, 1H), 7.60–7.51 (m, 1H), 7.51–7.39 (m, 2H), 7.22 (t, *J* = 7.8 Hz, 1H), 7.18–7.05 (m, 1H), 4.43 (ddd, *J* = 9.0, 7.6, 5.4 Hz, 1H), 3.98 (dd, *J* = 5.8, 2.1 Hz, 2H), 2.34 (s, 3H), 1.96–1.68 (m, 2H), 0.95 (t, *J* = 7.4 Hz, 3H). ^{13}C NMR (400 MHz, DMSO-d_6, δ) 173.02, 168.53, 167.12, 136.80, 135.13, 134.55, 131.78, 128.62, 128.05, 127.59, 127.10, 126.48, 122.97, 55.52, 43.39, 25.26, 20.69, 11.23. HRMS (ESI) m/z: $[M + H]^+$ calcd for $C_{20}H_{23}ClN_3O_3$, 388.1423; found, 388.1438.

(R)-N-(1-((2-((2-bromo-3-methylphenyl)amino)-2-oxoethyl)amino)-1-oxobutan-2-yl)benzamide (**SM4**) (97.17% purity, 25.6% yield) ^{1}H NMR (400 MHz, DMSO-d_6, δ) 9.28 (s, 1H), 8.54–8.43 (m, 2H), 7.95–7.86 (m, 2H), 7.54 (ddt, *J* = 8.8, 6.4, 1.7 Hz, 2H), 7.50–7.40 (m, 2H), 7.26 (t, *J* = 7.8 Hz, 1H), 7.21–7.14 (m, 1H), 4.45 (ddd, *J* = 9.1, 7.8, 5.3 Hz, 1H), 3.96 (d, *J* = 5.8 Hz, 2H), 2.37 (s, 3H), 1.88 (tq, *J* = 12.8, 6.4 Hz, 1H), 1.76 (ddq, *J* = 14.4, 9.0, 7.3 Hz, 1H), 0.94 (t, *J* = 7.4 Hz, 3H). ^{13}C NMR (400 MHz, DMSO-d_6, δ) 173.01, 168.44, 167.12, 138.86, 136.47, 134.55, 131.79, 128.63, 128.05, 127.87, 127.79, 123.54, 120.02, 55.48, 43.38, 25.29, 23.84, 11.25. HRMS (ESI) m/z: $[M + H]^+$ calcd for $C_{20}H_{23}BrN_3O_3$, 432.0918; found, 432.0937.

(R)-N-(1-((2-((3-fluoro-5-methylphenyl)amino)-2-oxoethyl)amino)-1-oxobutan-2-yl)benzamide (**SM5**) (97.28% purity, 14.6% yield) ^{1}H NMR (400 MHz, DMSO-d_6, δ) 9.84 (s, 1H), 8.61 (d, *J* = 6.9 Hz, 1H), 8.46 (t, *J* = 5.9 Hz, 1H), 7.99 (dt, *J* = 7.0, 1.4 Hz, 2H), 7.65–7.45 (m, 4H), 7.28 (s, 1H), 6.84–6.73 (m, 1H), 4.38 (dt, *J* = 8.4, 6.2 Hz, 1H), 4.02–3.87 (m, 2H), 2.33 (s, 3H), 1.98–1.75 (m, 2H), 1.01 (t, *J* = 7.4 Hz, 3H). ^{13}C NMR (101 MHz, DMSO-d_6, δ) 172.85, 168.55, 167.56,

163.76, 161.37, 140.91, 140.62, 134.34, 131.94, 128.68, 128.07, 115.75, 110.80, 103.72, 56.12, 43.31, 24.91, 21.55, 11.21. HRMS m/z(ESI): $[M + H]^+$ $C_{20}H_{23}FN_3O_3$, 372.1718; found, 372.1726.

(R)-N-(1-((2-((3-chloro-2-hydroxyphenyl)amino)-2-oxoethyl)amino)-1-oxobutan-2-yl)benzamide (**SM6**) (97.37% purity, 35.2% yield) ^{1}H NMR (400 MHz, DMSO-d_6, δ) 9.74 (s, 1H), 9.49 (s, 1H), 8.45 (d, J = 7.6 Hz, 1H), 8.36 (t, J = 5.8 Hz, 1H), 7.94–7.87 (m, 2H), 7.62–7.50 (m, 2H), 7.47 (dd, J = 8.2, 6.6 Hz, 2H), 7.16 (dd, J = 8.1, 1.5 Hz, 1H), 6.84 (t, J = 8.1 Hz, 1H), 4.41 (td, J = 8.4, 5.5 Hz, 1H), 4.07–3.90 (m, 2H), 1.89 (ddd, J = 13.2, 7.4, 5.6 Hz, 1H), 1.76 (ddd, J = 13.6, 8.9, 7.1 Hz, 1H), 0.95 (t, J = 7.4 Hz, 3H). ^{13}C NMR (400 MHz, DMSO-d_6, δ) 172.94, 169.32, 167.18, 144.93, 134.53, 131.81, 128.65, 128.50, 128.04, 126.02, 121.99, 121.89, 120.59, 55.56, 43.26, 25.26, 11.23. HRMS (ESI) m/z: $[M + H]^+$ calcd for $C_{19}H_{22}ClN_3O_3$, 390.1216; found, 390.1219.

Anti-PRV assay.

Cells and Virus.PK15 cells (archived in our laboratory[61]) were maintained in Dulbecco's Modified Eagle Medium (DMEM; No. 11965092, Gibco) supplemented with 10% fetal bovine serum (No. P30-3306, PANTM) and 1% penicillin-streptomycin (100X, No. BL505A, Biosharp) at 37°C. The PRV strain used was clinically isolated from Hubei Province in our previous work[44].

Cell antiviral assay. Confluent PK15 monolayers (80%) in 96-well plates (or into 24-well plates for CPE observation) were serum-starved for 4 hours using DMEM with 2% FBS after PBS washing. Cells were pre-treated with serially diluted minibinders or small molecules for 2 hours before PRV infection (MOI = 1). Post-infection (48 h), total DNA was extracted via phenol-chloroform (Solarbio), and PRV genomic copies were quantified 3-times with 2 × Taq Master Mix (Vazyme, Nanjing, China) by SYBR Green qPCR using gB-specific primers (**Table S1**). Viral inhibition was calculated as: Inhibition rate=(1-(number of virus copies in experimental group)/(number of virus copies in positive group))×100%.

PRV attachment assay. Following established methods[62], PK15 cells (70% confluency) were pre-incubated with **B1** (0.5 or 1.0 μM) or **SM1** (0.25 or 1.0 μM) for 2 hours. After compound removal, cells were infected with PRV (MOI = 1) in serum-free DMEM (37°C, 1 h). Post-infection washes with PBS removed unbound virus before qPCR quantification of cell-associated viral DNA.

PRV entry assay. Following established methods[62], Cells were first bound with PRV (MOI = 1) in serum-free DMEM (4°C, 1 h) to synchronize attachment. After cold PBS washes, **B1** (0.5 or 1.0 μM) or **SM1** (0.25 or 1.0 μM) in 2% FBS/DMEM was added during the 37°C entry phase (1 h). External virions were inactivated by pH 3.0 citrate buffer washes before qPCR analysis of internalized virus.

Cell viability assay.

Cell viability was determined by using the CCK-8 reagent assay (No. BL1055B, Biosharp). Briefly, PK15 cells were proceeded at 80% confluence in 96-well plates, and 12 h later, the cells were treated with various concentrations of inhibitors or 1% DMSO (control group). 72 h later, CCK-8 reagent was added with 10 μL per well and incubated at 37 ℃ for 2 h. The optical density was measured at a wavelength of 450 nm by Envision 2105, PerkinElmer. The results were plotted as % of cell viability in treated group compared to the control group. More detailed can be found in our previous work[29]. The CC_{50}s was fitted by GraphPad Prism 10.

Biolayer interferometry (BLI) assay.

Biotinlyated protein (0.1 mg/mL Avi-tag Nectin-1 IgV domain) was immobilized on streptavidin-coated sensor tips in buffer I (10 mM HEPES pH 7.4, 150 mM NaCl, 3 mM EDTA, 0.05% Tween 20 and 1% BSA) for 30 min. For **B1**, it were diluted in buffer II (PBS, 3 mM EDTA, 0.05% Tween 20 and 1% BSA) to indicated concentrations, while For **SM1 (**diluted in DMSO**)**, it were diluted in buffer III (PBS, 0.05% Tween 20) to indicated concentrations, sensor tips were sequentially dipped into buffer wells to run the line, and then were dipped into binder solutions for association. The tips went back into buffer wells for dissociation. The data were analyzed and processed using Octet Analysis Studio v.13.0.1.35.

Animals.

All animal procedures complied with institutional guidelines for care and use of laboratory animals and were approved by the Anima Ethic and Welfare Committee of Hubei University (approval number: 20250085).

Pharmacokinetic study for SM1.

Female kunming mice ((6–8 weeks old, fasted overnight) received a single intraperitoneal dose of **SM1**(30 mg/kg in 6 mg/mL, PEG200 solution). Blood samples (~ 60 µL) were collected via retro-orbital bleeding at 0.25, 0.5, 0.75, 1, 1.5, 2, 4, 6, 8, 12, and 24 h post-dose (n = 3 per timepoint) into heparinized tubes. Plasma was processed immediately, flash-frozen, and stored at -80°C pending LC-MS/MS analysis. Terminal sampling at 24 h was followed by cervical dislocation. Detailed methodology (calibration, chromatography, PK calculations) is in **Supplementary information.**

Pharmacodynamic study for **B1** *and* **SM1**.

Female Kunming mice (6–8 weeks) housed under specific pathogen-free conditions were challenged with PRV (5×10^7 copies in 100 µL PBS) via intramuscular injection. Treatment groups received either **B1** (PBS solution, 6 mg/kg), **SM1** (**SM1**-saturated DMSO solution dissolved in corn oil, 30 mg/kg) or solvent vehicle control via intraperitoneal injection twice daily (BID) for 7 days. Animals surviving to day 7.5 were euthanized by cervical dislocation, with brain tissues collected and homogenized in PBS (1 g:2 mL w/v). Viral loads in homogenates were quantified by qPCR using the gB primers and methodology.

RNA isolation and real-time qPCR assay.

Brain tissues for **SM1**-treated and vehicle control were homogenized in RNA isolater Total RNA Extraction Reagent (R401-01, Vazyme Biotech). Total RNA was isolated, reverse transcribed into cDNA using ABScript III RT Master Mix (RK20429, ABclonal Technology), and analyzed 3-times by real-time qPCR using Universal SYBR Green Fast qPCR Mix (RK21203, ABclonal Technology). The specific primers for TNF-α, IL1-β, IL-6, β-actin (used as the house-keeping gene) were shown in **Table S1**. Relative gene expression was analyzed using the 2^(-ΔΔCt) method.

H&E staining

Brain tissues from **SM1**-treated and control mice were fixed in 4% paraformaldehyde overnight, embedded in paraffin sectioned, dehydrated, and stained with hematoxylin and eosin (H&E).

UMAP Analysis.

UMAP plots were created using the umap-learn Python library with default parameters and Euclidean distance metric to reduce dimensions from three (TC, Vina score, QED) to two. The ‘spectral’ color map was used in matplotlib. QED properties were computed using RDKit functions, UMAP plots were created with n_neighbors = 15, min_dist = 0.1.

Statistical analysis

Statistical analysis was performed using Graphpad Prism 10. Data are all indicated as mean ± SD. Survival curves were obtained using the Kaplan-Meier method and compared by the log-rank test. An unpaired two-tailed t-test or two-way ANOVA with a Tukey post hoc test was performed for statistical analyses. The level of significance was set at ***p < 0.005, **p < 0.01. *p < 0.05.

Data and Software Availability

The code for XREINVENT are available on Github (https://github.com/weilin199204/xdalgorithm_XtalPi_copy). The input files and output files are provided in the Zenodo (https://zenodo.org/records/16986879).

Declarations

Data and Software Availability

The code for XREINVENT are available on Github (https://github.com/weilin199204/xdalgorithm_XtalPi_copy). The input files and output files are provided in the Zenodo (https://zenodo.org/records/16986879).

Acknowledgments

This work was supported by Key Research and Development Progarm of Wuhan (2025020602030105), Hubei Provincial Natural Science Foundation of China (2024AFB465), Major Special Projects for the Development of Agricultural Microbial Industry in Hubei Province (NYWSWZX2025-2027-03; NYWSWZX2025-2027-10), State Key Laboratory Open Project (SKLBEE2022007) from State Key Laboratory of Biocatalysis and Enzyme Engineering and Enzyme Engineering. We thank HPC center at State Key Laboratory of Biocatalysis and Enzyme Engineering for cloud computing support.

Author information contributions

L. W.: formal analysis, funding acquisition, methodology, resources, software, visualization, writing – original draft, writing – review & editing; Y. H.: formal analysis, methodology, validation, visualization, writing – original draft, writing – review & editing; P. C.: formal analysis, methodology, validation, writing – original draft, writing – review & editing; Y. C.: formal analysis, validation, visualization, writing – original draft, writing – review & editing; K. W.: formal analysis, validation, writing – original draft, writing – review & editing, J. W.: funding acquisition, methodology, supervision, writing – original draft, writing – review & editing; B. X.: formal analysis, software, writing – original draft, writing – review & editing; H. F.: visualization, writing – original draft, writing – review & editing; K. M.: formal analysis, visualization, writing – original draft, writing – review & editing; Z. W., M. G., Z. L., G. W., Y. Y., Y, L., & W. Z.: validation, writing – review & editing; H. X.: validation; Z. W.: Funding acquisition, Supervision, Writing – review & editing.

Ethics declarations

Competing interests

The authors declare no competing interests.

Supplementary information.

More computational and experimental methods, details of the results, methods of chemical synthesis and ^{1}H NMR, ^{13}C NMR spectroscopy and HRMS.

The poses files, and the max TCs compared to the ChEMBL_36 database, Vina scores for the 20,000 compounds generated in this work.

References

1. Gao, X. *et al.* Serological Investigation of Porcine Pseudo-rabies on Intensive Swine Farms From 2012 to 2017 in China. *Chin. J. Ani. Infect. Dis.* 28, 87–90 (2020).
2. Zhao, P. *et al.* Epidemiological Investigation, Risk Factors, Spatial-Temporal Cluster, and Epidemic Trend Analysis of Pseudorabies Virus Seroprevalence in China (2017 to 2021). *Microbiol. Spectrum* 11, e05297-05222 (2023).
3. Xu, G. *et al.* Acute Retinal Necrosis Associated with Pseudorabies Virus Infection: A Case Report and Literature Review. *Ocul. Immunol. Inflamm.* 32, 594–601 (2024).
4. Liu, Q. *et al.* A Novel Human Acute Encephalitis Caused by Pseudorabies Virus Variant Strain. *Clin. Infect. Dis.* 73, e3690-e3700 (2021).
5. Geraghty, R.J., Krummenacher, C., Cohen, G.H., Eisenberg, R.J. & Spear, P.G. Entry of Alphaherpesviruses Mediated by Poliovirus Receptor-Related Protein 1 and Poliovirus Receptor. *Science* 280, 1618–1620 (1998).
6. Simpson, S.A. *et al.* Nectin-1/HveC Mediates herpes simplex virus type 1 entry into primary human sensory neurons and fibroblasts. *J. Neurovirol.* 11, 208–218 (2005).
7. Menotti, L. *et al.* The murine homolog of human nectin1δ serves as a species nonspecific mediator for entry of human and animal alphaherpesviruses in a pathway independent of a detectable binding to gD. *Proc. Natl. Acad. Sci. U. S. A.* 97, 4867–4872 (2000).
8. Petermann, P. *et al.* Entry mechanisms of herpes simplex virus 1 into murine epidermis: involvement of nectin-1 and herpesvirus entry mediator as cellular receptors. *J. Virol.* 89, 262–274 (2015).
9. Manoj, S., Jogger, C.R., Myscofski, D., Yoon, M. & Spear, P.G. Mutations in herpes simplex virus glycoprotein D that prevent cell entry via nectins and alter cell tropism. *Proc. Natl. Acad. Sci. U. S. A.* 101, 12414–12421 (2004).
10. Zhou, Z.H. *et al.* Structural basis of nectin-1 recognition by pseudorabies virus glycoprotein D. *PLoS Pathog.* 13, e1006314 (2017).
11. Connolly, S.A. *et al.* Glycoprotein D homologs in herpes simplex virus type 1, pseudorabies virus, and bovine herpes virus type 1 bind directly to human HveC(nectin-1) with different affinities. *Virology* 280, 7–18 (2001).
12. Milne, R.S., Connolly, S.A., Krummenacher, C., Eisenberg, R.J. & Cohen, G.H. Porcine HveC, a member of the highly conserved HveC/nectin 1 family, is a functional alphaherpesvirus receptor. *Virology* 281, 315–328 (2001).
13. Spear, P.G. *et al.* Different receptors binding to distinct interfaces on herpes simplex virus gD can trigger events leading to cell fusion and viral entry. *Virology* 344, 17–24 (2006).
14. Campadelli-Fiume, G., Cocchi, F., Menotti, L. & Lopez, M. The novel receptors that mediate the entry of herpes simplex viruses and animal alphaherpesviruses into cells. *Rev. Med. Virol.* 10, 305–319 (2020).
15. Wei, L. *et al.* De novo design mini-binder proteins targeting the glycoproteins D to inhibit PRV replication in PK15 cells. *International Journal of Biological Macromolecules* 315 (2025).
16. Dauparas, J. *et al.* Robust deep learning–based protein sequence design using ProteinMPNN. *Science* 378, 49–56 (2022).

17. Watson, J.L. *et al.* De novo design of protein structure and function with RFdiffusion. *Nature* 620, 1089–1100 (2023).
18. Cao, L. *et al.* De novo design of picomolar SARS-CoV-2 miniprotein inhibitors. *Science* 370, 426–431 (2020).
19. Ming, K. *et al.* De novo design of a protein binder against Staphylococcus enterotoxin B. *Int. J. Biol. Macromol.* 257, 128666 (2024).
20. Ming, K. *et al.* De novo design of mini-binder proteins against IL-2 receptor beta chain. *Int. J. Biol. Macromol.* 276, 133834 (2024).
21. Huang, B. *et al.* De novo design of miniprotein antagonists of cytokine storm inducers. *Nat. Commun.* 15, 7064 (2024).
22. Berger, S. *et al.* Preclinical proof of principle for orally delivered Th17 antagonist miniproteins. *Cell* 187, 4305–4317.e4318 (2024).
23. Beck, H., Härter, M., Haß, B., Schmeck, C. & Baerfacker, L. Small molecules and their impact in drug discovery: A perspective on the occasion of the 125th anniversary of the Bayer Chemical Research Laboratory. *Drug Discovery Today* 27, 1560–1574 (2022).
24. Wang, H. in IMMpress Magazine (https://www.immpressmagazine.com/small-vs-big-understanding-the-differences-between-small-molecule-drugs-and-biologic-drugs/; 2019).
25. AstraZeneca (https://www.astrazeneca.com/r-d/next-generation-therapeutics/small-molecule.html; 2024).
26. Stelzl, U. *et al.* A human protein-protein interaction network: a resource for annotating the proteome. *Cell* 122, 957–968 (2005).
27. Rual, J.F. *et al.* Towards a proteome-scale map of the human protein-protein interaction network. *Nature* 437, 1173–1178 (2005).
28. C., G.A. *et al.* Functional organization of the yeast proteome by systematic analysis of protein complexes. *Nature* 415, 141–147 (2002).
29. Yan, R. *et al.* Structural basis for the recognition of SARS-CoV-2 by full-length human ACE2. *Science* 367, 1444–1448 (2020).
30. Lu, H. *et al.* Recent advances in the development of protein-protein interactions modulators: mechanisms and clinical trials. *Signal Transduct Target Ther* 5, 213 (2020).
31. Smith, M.C. & Gestwicki, J.E. Features of protein–protein interactions that translate into potent inhibitors: topology, surface area and affinity. *Expert Reviews in Molecular Medicine* 14 (2012).
32. Scott, D.E., Bayly, A.R., Abell, C. & Skidmore, J. Small molecules, big targets: drug discovery faces the protein-protein interaction challenge. *Nat Rev Drug Discov* 15, 533–550 (2016).
33. Ni, D., Lu, S. & Zhang, J. Emerging roles of allosteric modulators in the regulation of protein-protein interactions (PPIs): A new paradigm for PPI drug discovery. *Med Res Rev* 39, 2314–2342 (2019).
34. Arkin, M.R., Tang, Y. & Wells, J.A. Small-molecule inhibitors of protein-protein interactions: progressing toward the reality. *Chem Biol* 21, 1102–1114 (2014).
35. Nero, T.L., Morton, C.J., Holien, J.K., Wielens, J. & Parker, M.W. Oncogenic protein interfaces: small molecules, big challenges. *Nat Rev Cancer* 14, 248–262 (2014).
36. Milroy, L.G., Grossmann, T.N., Hennig, S., Brunsveld, L. & Ottmann, C. Modulators of protein-protein interactions. *Chem Rev* 114, 4695–4748 (2014).
37. Aeluri, M. *et al.* Small molecule modulators of protein-protein interactions: selected case studies. *Chem Rev* 114, 4640–4694 (2014).

38. Ivanov, A.A., Khuri, F.R. & Fu, H. Targeting protein-protein interactions as an anticancer strategy. *Trends Pharmacol Sci* 34, 393–400 (2013).
39. Winter, A. *et al.* Biophysical and computational fragment-based approaches to targeting protein-protein interactions: applications in structure-guided drug discovery. *Quarterly reviews of biophysics* 45, 383–426 (2012).
40. Sutton, R.S. & Barto, A.G. *Reinforcement Learning: An Introduction*. (The MIT Press, 2015).
41. Blaschke, T., Engkvist, O., Bajorath, J. & Chen, H. Memory-assisted reinforcement learning for diverse molecular de novo design. *Journal of Cheminformatics* 12 (2020).
42. Liu, X., Ye, K., van Vlijmen, H.W.T., Ijzerman, A.P. & van Westen, G.J.P. An exploration strategy improves the diversity of de novo ligands using deep reinforcement learning: a case for the adenosine A2A receptor. *Journal of Cheminformatics* 11 (2019).
43. Olivecrona, M., Blaschke, T., Engkvist, O. & Chen, H. Molecular de-novo design through deep reinforcement learning. *J Cheminform* 9, 48 (2017).
44. Wei, L. *et al.* Design of the Inhibitors for Pseudorabies Virus Replication by Reinforcement Learning from HSV-1 DNA Polymerase Inhibitors. *ACS Omega* 10, 3389–3397 (2025).
45. Wei, L. *et al.* Hit Identification Driven by Combining Artificial Intelligence and Computational Chemistry Methods: A PI5P4K-β Case Study. *Journal of chemical information and modeling* 63, 5341–5355 (2023).
46. Cao, L. *et al.* Design of protein-binding proteins from the target structure alone. *Nature* 605, 551–560 (2022).
47. Jumper, J. *et al.* Highly accurate protein structure prediction with AlphaFold. *Nature* 596, 583–589 (2021).
48. Cao, L. *et al.* De novo design of picomolar SARS-CoV-2 miniprotein inhibitors. *Science* 370, 426–431 (2020).
49. Zhang, N. *et al.* Binding of herpes simplex virus glycoprotein D to nectin-1 exploits host cell adhesion. *Nat. Commun.* 2, 577 (2011).
50. Rego, N.B., Xi, E. & Patel, A.J. Identifying hydrophobic protein patches to inform protein interaction interfaces. *Proceedings of the National Academy of Sciences* 118, e2018234118 (2021).
51. Cao, L. *et al.* Design of protein-binding proteins from the target structure alone. *Nature* 605, 551–560 (2022).
52. Zdrazil, B. *et al.* The ChEMBL Database in 2023: a drug discovery platform spanning multiple bioactivity data types and time periods. *Nucleic Acids Research* 52, D1180-D1192 (2024).
53. Davies, M. *et al.* ChEMBL web services: streamlining access to drug discovery data and utilities. *Nucleic Acids Research* 43, W612-W620 (2015).
54. Rogers, D. & Hahn, M. Extended-Connectivity Fingerprints. *J. Chem. Inf. Model.* 50, 742–754 (2010).
55. Chen, Y. *et al.* The Co-application of Nectin-1 and PRV gD Monoclonal Antibodies: An Effective Approach to Block Pseudorabies Virus Invasion. *J. Virol. Met.* (2025).
56. Schneidman-Duhovny, D., Inbar, Y., Nussinov, R. & Wolfson, H.J. PatchDock and SymmDock: servers for rigid and symmetric docking. *Nucleic Acids Research* 33, W363-W367 (2005).
57. Chung, J., Gulcehre, C., Cho, K. & Y., B. Empirical Evaluation of Gated Recurrent Neural Networks on Sequence Modeling. *arXiv:1412.3555v1* (2014).
58. Goodfellow, I.J., Mirza, M., Xiao, D., Courville, A. & Bengio, Y. An empirical investigation of catastrophic forgetting in gradient-based neural networks. *arXiv:1312.6211v3* (2013).
59. Wei, L. *et al.* Hit Identification Driven by Combining Artificial Intelligence and Computational Chemistry Methods: A PI5P4K-β Case Study. *J. Chem. Inf. Model.* 63, 5341–5355 (2023).

60. Blaschke, T. *et al.* REINVENT 2.0: An AI Tool for De Novo Drug Design. *J. Chem. Inf. Model.* 60, 5918–5922 (2020).
61. Tang, B., Liang, H., Zhao, P. & Wei, Z. miR-194b-3p partially inhibits Streptococcus equi subsp. zooepidemicus adherence to PK15 cells. *Vet. Microbiol.* 210, 38–42 (2017).
62. Bo, Z. *et al.* Ginkgolic acid inhibits the replication of pseudorabies virus in vitro and in vivo by suppressing the transcription of viral late genes. *Res Vet Sci* 164, 105033 (2023).

Figures

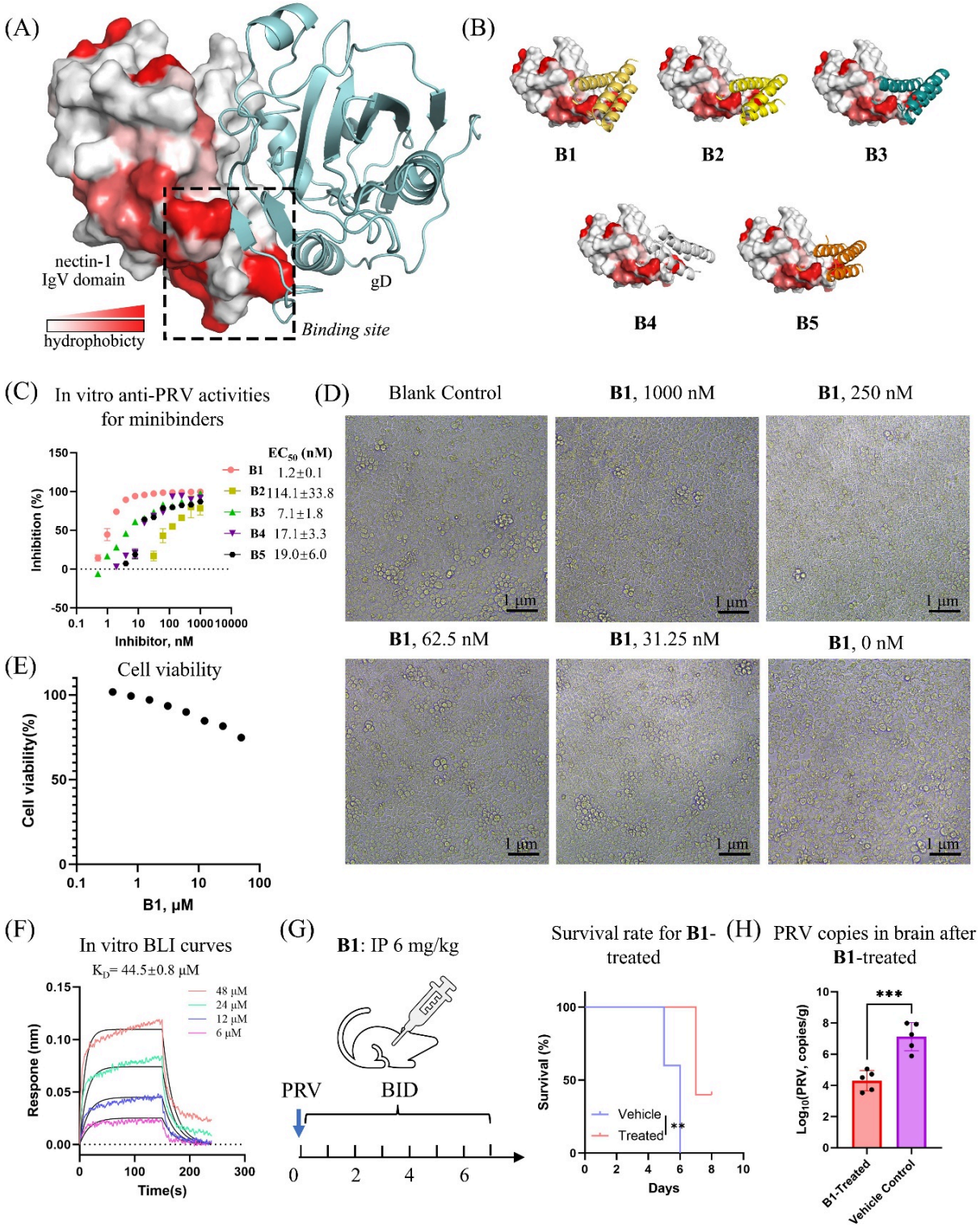


Figure 1

(A) Structure of the porcine Nectin-1 IgV domain in complex with PRV gD (PDB ID: 5X5W), highlighting the hydrophobic surface targeted for minibinder design. (B) Computational models of the designed minibinders bound to the Nectin-1 IgV domain hydrophobic patch. (C) *In vitro* concentration-response curves of minibinders against PRV infection in PK15 cells. (D) PK15 cells were pre-treated with **B1**(31.25 nM–1 μM) for 2 h, and then infected them with PRV. At 48 h, CPE results were observed. Images were representative of results obtained from three independent experiments, scale bars = 1 μm. (E) *In vitro* cell viabilities of **B1**. (F) BLI measurements indicate high-affinity of **B1**

binding to Nectin-1 IgV domain. (G) Survival rates of mice treated with **B1** (6 mg/kg, BID, IP, n=5) or vehicle control following PRV challenge. Survival curves were obtained using the Kaplan-Meier method and compared by the log-rank test. (H) PRV copies per gram of brain tissue in mice treated with **B1**or vehicle control at study endpoint. Statistical significance: ***p <0.005, determined by two-tailed t test assuming equal variance (GraphPad Prism 10).

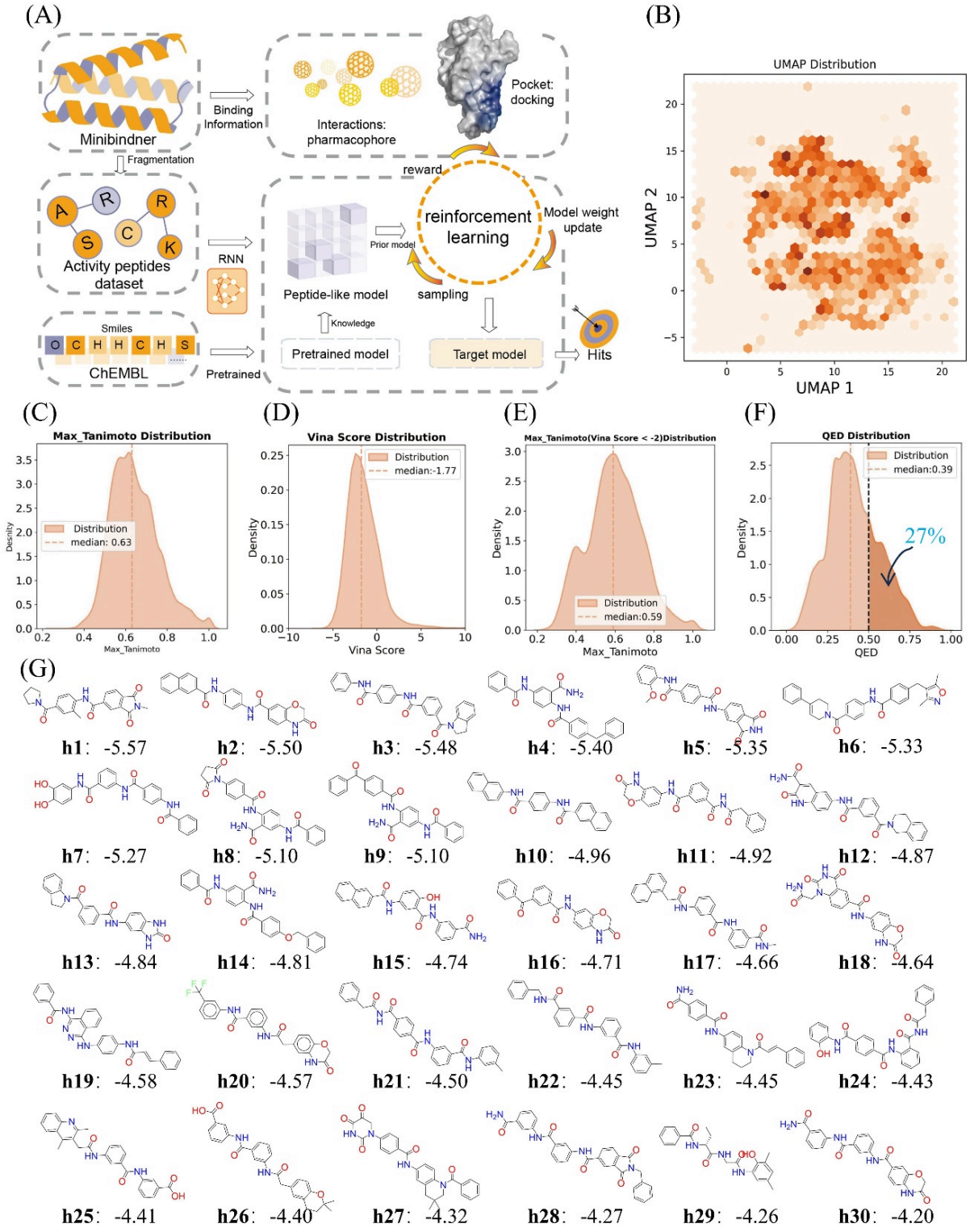


Figure 2

(A)The protocol for converting minibinder to small molecule inhibitors. (B)UMAP. Visualization of the chemical space. Each hexagon is a molecule distribution colored by the density. (C)The distribution of max TCs for all generated

compounds. (D) The distribution of Vina scores after docking for all generated compounds. (E) The distribution of max TCs for the generated compounds with Vina Score <-2 kcal/mol.(F) The distribution of QEDs for all generated compounds. (G) The top 30 hits compounds from the deep RL protocol after docking and visual inspection. The label for echo compounds contains the Vina score (kcal/mol).

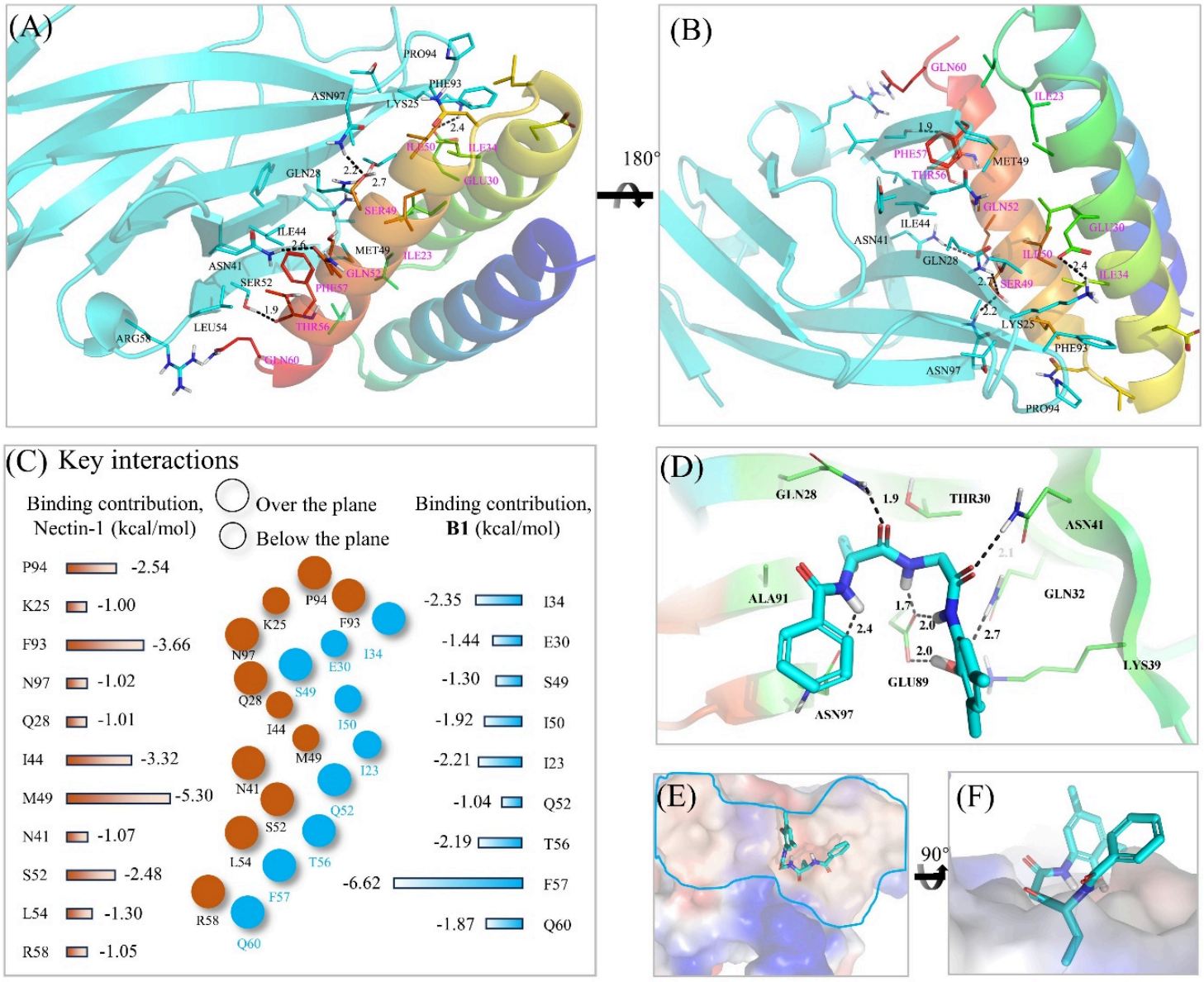


Figure 3

Key interactions guiding small-molecule design. (A-B) Predicted binding pose of **B1** (e.g., from MD representative structure) complexed with the Nectin-1 IgV domain, highlighting interface residues. The residues of **B1** were label by rose and the residues of Nectin-1 were label by black. Black dashed lines indicate hydrogen bonds. (C) Residue energy decomposition plot (from MM/GBSA) illustrating the contribution of key residues in Nectin-1 and **B1** to the binding free energy. (D) Predicted binding pose of the lead small-molecule **h29** within the Nectin-1 binding site from AutoDock Vina. Black dashed lines indicate hydrogen bonds. (E) Surface representation showing **h29** bound at the Nectin-1:gD interface, Electrostatic surface potential map of the Nectin-1:gD interface was surrounded by cyan line, with blue indicating positive and red indicating negative charge. (F) The **h29** "suspended" above the surface.

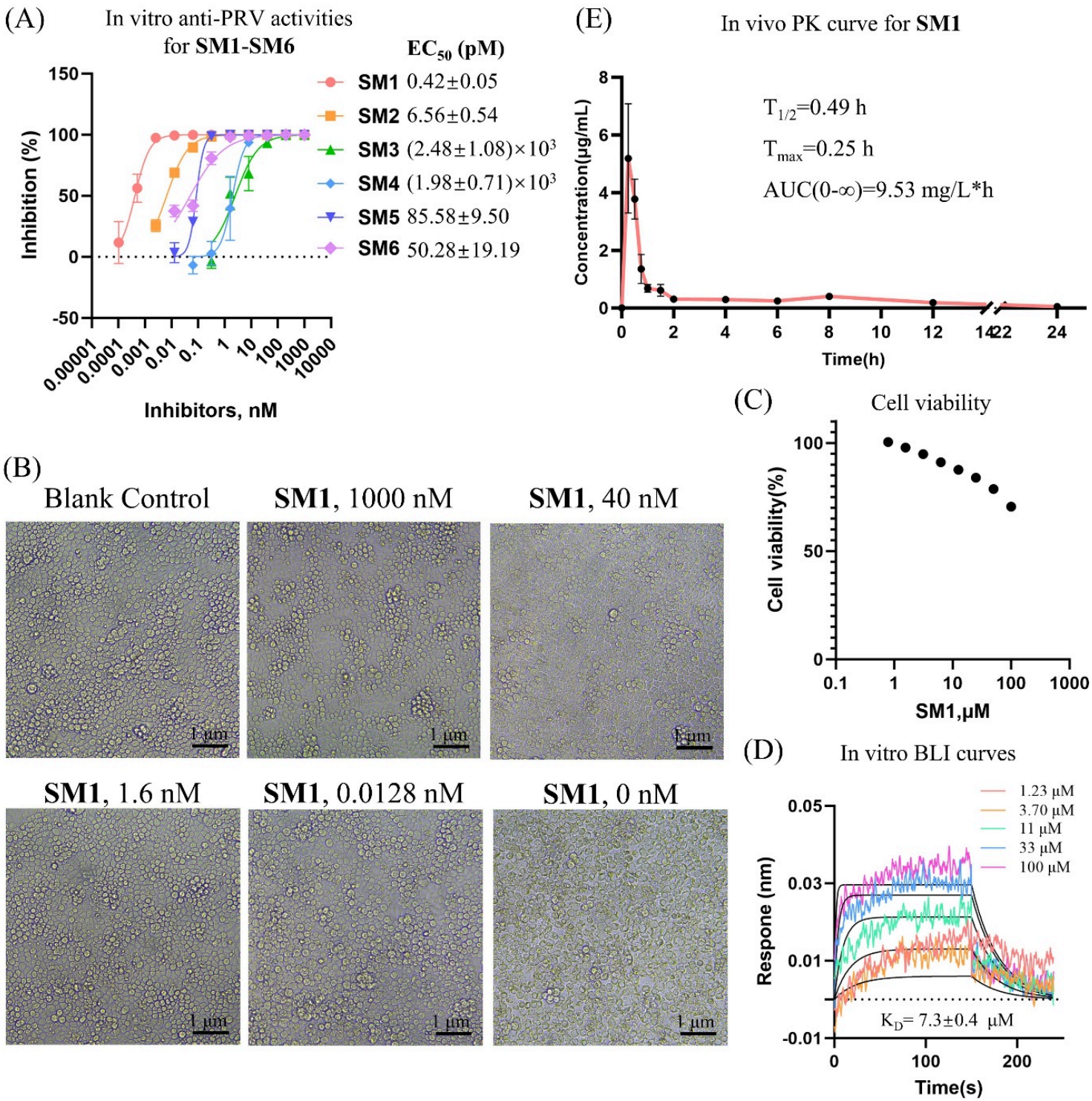


Figure 4

(A) *In vitro* concentration-response curves of small molecules (**SM1-SM6**) against PRV infection in PK15 cells. (n=3) (B) PK15 cells were pre-treated with **SM1** (12.8 pM–1 μM) for 2 h, and then infected them with PRV. At 48 h, CPE results were observed. Images were representative of results obtained from three independent experiments, scale bars = 1 μm. (C) *In vitro* cell viabilities of **SM1**. (n=3) (D) BLI measurements indicate high-affinity of **SM1** binding to Nectin-1 IgV domain. (E) Mean plasma concentration-time profile of **SM1**in male Kunming mice after a single IP dose (30 mg/kg; n=3).

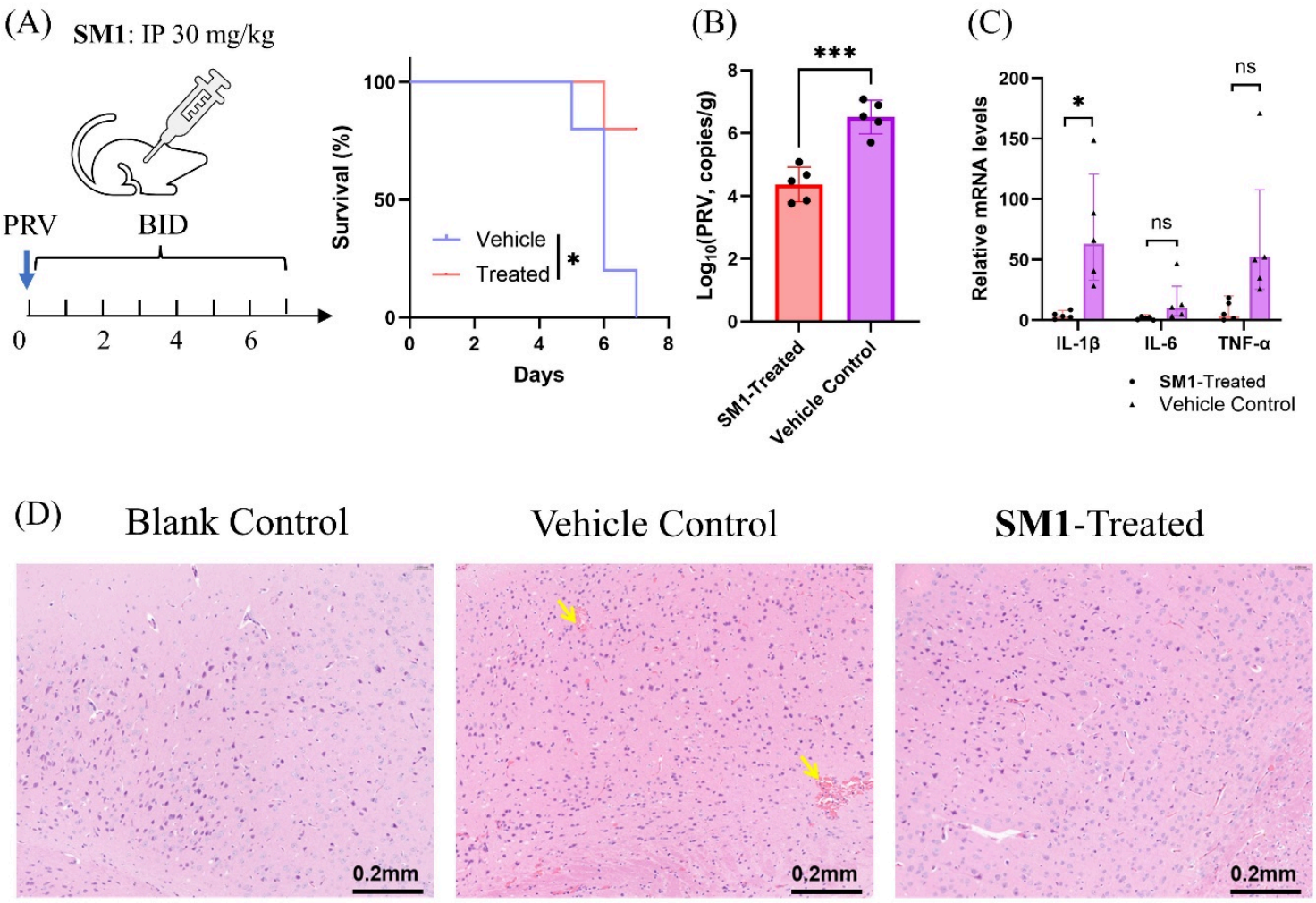


Figure 5

(A) Survival rates of mice treated with **SM1** (30 mg/kg, BID, IP, n=5) or vehicle control following PRV challenge. (B) PRV copies per gram of brain tissue in mice treated with **SM1** or vehicle control at study endpoint. (C) The expression of IL-1β, IL-6, and TNF-α, in brain tissue in mice treated with **SM1**or vehicle control at study endpoint. Statistical significance: ***p <0.005, **p <0.01. *p <0.05. ns = not significant (p > 0.05); determined by two-way ANOVA with a Tukey post hoc test (GraphPad Prism 10). (D) The representative H&E staining of brain tissue in mice treated with **SM1**or vehicle control at study endpoint.

Supplementary Files

This is a list of supplementary files associated with this preprint. Click to download.

- results.zip
- nectinSI9.docx
- MLreportingsummary16.pdf